Adaptive Control and the NASA X-15-3 Flight Revisited

Adaptive Control and the NASA X-15-3 Flight Revisited

NASA DRYDEN FLIGHT RESEARCH CENTER (NASA-DFRC)

LESSONS LEARNED AND LYAPUNOV-STABILITY-BASED DESIGN

ZACHARY T. DYDEK,
ANURADHA M. ANNASWAMY,
and EUGENE LAVRETSKY

Decades after the first hypersonic vehicles pushed the boundaries of aerospace technology and research, high-performance aircraft continue to be the subject of considerable research interest. A new generation of hypersonic vehicles offers a far more effective way of launching small satellites or other vehicles into low-Earth orbit than expendable rockets. Additionally, these aircraft facilitate quick response and global strike capabilities. High-performance missions involving the X-15 in the 1950s and 1960s and the X-43A in the 2000s pushed the boundaries of aircraft speed and altitude, setting world records. These aircraft also served as platforms for cutting-edge research in propulsion, hypersonic stability, and control, as well as supporting technologies that enabled the design and operation of subsequent aircraft and spacecraft. This article examines the role of control in NASA's X-15 program and, in particular, the X-15-3, which used adaptive control. The X-15 aircraft is depicted in Figure 1.

Control of hypersonic vehicles is challenging due to the changes in the aircraft dynamics as the maneuver takes the aircraft over large flight envelopes. Three hypersonic planes, the X-15-1, X-15-2, and X-15-3, were flown as a part of the NASA X-15 program. The X-15-1 and X-15-2 were equipped with a fixed-gain stability augmentation system. In contrast, the X-15-3 was one of the earliest aircraft to feature an adaptive control scheme. The Honeywell MH-96 self-adaptive controller adjusted control

Digital Object Identifier 10.1109/MCS.2010.936292

1066-033X/10/$26.00©2010IEEE

parameters online to enforce performance of the aircraft throughout the flight envelope.

Preliminary design work for the X-15 started in 1955, and the program recorded nearly 200 successful flights from 1959 to 1968. The program is largely considered to be one of NASA's most successful, despite the fatal accident that occurred on November 15, 1967 with the X-15-3. According to [1], the events that led to the accident are as follows. Shortly after the aircraft reached its peak altitude, the X-15-3 began a sharp descent, and the aircraft entered a Mach 5 spin. Although the pilot recovered from the spin, the adaptive controller began a limit cycle oscillation, which prevented it from reducing the pitch gain to the appropriate level. Consequently, the pilot was unable to pitch up, and the aircraft continued to dive. Encountering rapidly increasing dynamic pressures, the X-15-3 broke apart about 65,000 feet above sea level.

FIGURE 1 The USAF X-15 aircraft in flight. The X-15 program recorded nearly 200 successful flights from 1959 to 1968 and set numerous records for manned aircraft, including maximum altitude and maximum velocity. The wingspan of the X-15 is approximately 22 feet, and the length from tip to tail is approximately 50 feet. The X-15 aircraft is powered by an XLR-99 rocket engine, which generates up to 57,000 lb of force. The aircraft has 3 main control surfaces, namely, a combined pitch/roll elevon on each wing as well as a large rudder. (Photo courtesy of NASA Dryden Historical Aircraft Photo Collection.)

The field of adaptive control began with the motivation that a controller that can adjust its parameters online could generate improved performance over a fixed-parameter counterpart. Subsequently, sobering lessons of tradeoffs between stability and performance directed the evolution of the field toward the design, analysis, and synthesis of stable adaptive systems. Various adaptive control methods have been developed for controlling linear and nonlinear dynamic systems with parametric and dynamic uncertainties [2]–[35].

With the benefit of hindsight and subsequent research, we revisit the events of 1967 by examining "how and what if" scenarios. Keeping in mind the lessons learned from the X-15 and additional programs [27], [36]–[38], we pose the question "What if we were to design an adaptive flight control system for the X-15-3 today?" To answer this question, we analyze the X-15-3 aircraft dynamics and the Honeywell MH-96 adaptive controller in an effort to better understand how the sequence of events and the interplay between the controller and the aircraft dynamics might have led to the instability and resulting crash. We follow this discussion with a depiction of a Lyapunov-stability-based adaptive controller that incorporates gain scheduling and accommodates actuator magnitude saturation, which we denote as the gain-scheduled, magnitude-saturation-accommodating, Lyapunov-stability-based (GMS-LS) adaptive controller. We then present results that might accrue if the GMS-LS adaptive control strategy were to be adopted for the X-15-3.

The original MH-96 controller consisted of analog electrical modules and mechanical linkages. This control system was designed and tested using a fixed-base flight simulator, which included hardware components as well as a bank of analog computers to simulate the nonlinear X-15 aircraft dynamics [39]. To evaluate the MH-96 and GMS-LS adaptive controllers, a digital version of the nonlinear six-degree-of-freedom aircraft model is formulated using aerodynamic data from various sources. Additionally, parametric uncertainty and nonlinearity in the form of actuator saturation are included. The GMS-LS adaptive controller [2], [5], [7] is designed using this aircraft model. A digital version of the MH-96 adaptive controller is also synthesized based on the descriptions in [40]–[44], which we denote as the reconstructed MH-96. With this aircraft model, we compare the MH-96 and the GMS-LS adaptive controller in the context of the reported accident of the X-15-3.

THE MH-96 ADAPTIVE CONTROLLER AND THE 1967 INCIDENT

The design intent for the MH-96 adaptive controller was to achieve a high level of performance throughout the flight envelope. Toward that end, it was observed [41] that the forward loop gain would need to be kept as high as possible while maintaining stability at all times. Since the X-15 aircraft moves rapidly between operating conditions during the course of its maneuvers, rapid changes in the controller gains are required. Therefore, a control design that continually adjusts these gains is desired. To accomplish this behavior, the system maintains a limit cycle oscillation at the natural frequency of the servoactuator loop. When the amplitude of this limit cycle becomes large, the gains are reduced to maintain stability. Otherwise, the gains are increased. In this manner, the gains are to be kept as high as possible while maintaining system stability throughout the entire flight envelope. In practice, due to the nature of the gain adjustment laws, the gain value often lagged behind the ideal setting [40]. Despite this issue, the pilot satisfaction ratings for the MH-96 controller were equal to or higher than those of their linear counterparts, which employed a standard stability augmentation system with pilot-selectable gains [45]. The improved performance was especially noticeable during re-entry, when changes in the flight condition were most dramatic [40], [44], [46]. In addition to the

performance advantages, the adaptive controller requires no external gain scheduling and therefore could be designed and implemented quickly and efficiently.

Modeling the X-15

The X-15 aircraft simulation model consists of the equations of motion, aerodynamics, actuator dynamics, actuator saturation, and sensor dynamics. These five subsystems are shown in Figure 2. The overall control architecture, also shown in Figure 2, includes multiple feedback loops. Each subsystem is described in detail below.

Equations of Motion

The conservation and kinematic equations describe the evolution of the aircraft velocities U, V, and W in the body-fixed frame; the roll, pitch, and yaw rates p, q, and r in the body-fixed frame; as well as the Euler angles ϕ, θ, and ψ [47]. These equations are given by

$$\dot{U} = g\frac{X}{w} - g\sin\theta - qW + rV, \tag{1}$$

$$\dot{V} = g\frac{Y}{w} + g\cos\theta\sin\phi - rU + pW, \tag{2}$$

$$\dot{W} = g\frac{Z}{w} + g\cos\theta\cos\phi + qU - pV, \tag{3}$$

$$\dot{p} = \frac{I_{zz}}{I_D}[L + I_{xz}pq - (I_{zz} - I_{yy})qr] + \frac{I_{xz}}{I_D}[N - I_{xz}qr - (I_{yy} - I_{xx})pq], \tag{4}$$

$$\dot{q} = \frac{1}{I_{yy}}[M - (I_{xx} - I_{zz})pr - I_{xz}(p^2 - r^2)], \tag{5}$$

$$\dot{r} = \frac{I_{xz}}{I_D}[L + I_{xz}pq - (I_{zz} - I_{yy})qr] + \frac{I_{xx}}{I_D}[N - I_{xz}qr - (I_{yy} - I_{xx})pq], \tag{6}$$

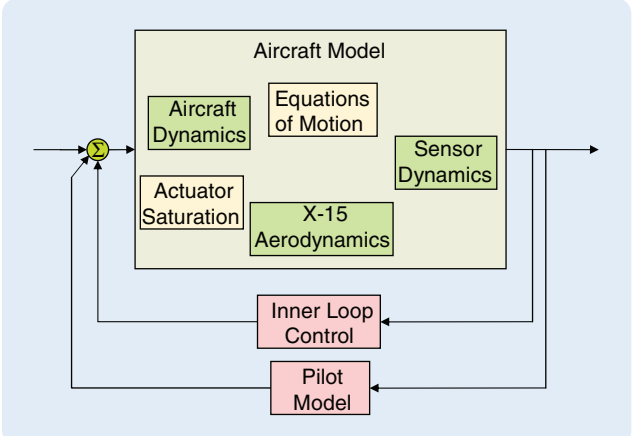

FIGURE 2 The six-degree-of-freedom X-15 aircraft model. The aircraft model is comprised of several subsystems, some of which are specific to the X-15 platform. The multiloop control structure consists of an inner-loop controller for the fast longitudinal and lateral dynamics as well as a pilot model for the slow states such as altitude and speed.

$$\dot{\phi} = p + q\sin\phi\tan\theta + r\cos\phi\tan\theta, \tag{7}$$

$$\dot{\theta} = q\cos\phi - r\sin\phi, \tag{8}$$

$$\dot{\psi} = (q\sin\phi + r\cos\phi)\sec\theta, \tag{9}$$

where $I_D = I_{xx}I_{zz} - I_{xz}^2$. X, Y, and Z are the aerodynamic forces on the aircraft in the body-fixed $x-$, $y-$, and $z-$ axes, and L, M, and N are the aerodynamic moments about the $x-$, $y-$, and $z-$axes. The values of the aircraft weight w, the moments of inertia I_{xx}, I_{yy}, and I_{zz}, as well as the product of inertia I_{xz} can be found in Table 1.

In addition to the conservation and kinematic equations (1)–(9), the navigation equations

$$\dot{x} = U\cos\theta\cos\psi + V(-\cos\phi\sin\psi + \sin\phi\sin\theta\cos\psi) + W(\sin\phi\sin\psi + \cos\phi\sin\theta\cos\psi), \tag{10}$$

$$\dot{y} = U\cos\theta\sin\psi + V(\cos\phi\cos\psi + \sin\phi\sin\theta\sin\psi) + W(-\sin\phi\cos\psi + \cos\phi\sin\theta\sin\psi), \tag{11}$$

$$\dot{h} = U\sin\theta - V\sin\phi\cos\theta - W\cos\phi\cos\theta, \tag{12}$$

determine x and y, the positions of the aircraft in the north and east directions, respectively, as well as the altitude h.

It is convenient to replace the body-fixed velocities with the true airspeed V_T, the angle of attack α, and the sideslip angle β. Since the X-15 is a hypersonic aircraft, the wind- and gust-induced effects are negligible. We can therefore calculate true airspeed, angle of attack, and sideslip angle from the body-fixed velocities as

$$V_T = (U^2 + V^2 + W^2)^{1/2}, \tag{13}$$

$$\tan\alpha = \frac{W}{U}, \tag{14}$$

$$\sin\beta = \frac{V}{V_T}. \tag{15}$$

Using (13)–(15), the aircraft dynamics are written in terms of the state vector

$$X_t = [V_T \ \alpha \ \beta \ p \ q \ r \ \phi \ \theta \ \psi \ x \ y \ h]^T. \tag{16}$$

TABLE 1 Simulation parameter values. These parameters describe the physical properties of the simulated X-15-3 aircraft, as well as the reconstructed MH-96 and pilot model.

S	200 ft^2	k_a	1	k_{r_0}	−0.05
b_{ref}	22.36 ft	k_{d1}	−0.5	k_{r_1}	0.1
C_{ref}	10.27 ft	k_{d2}	0.2	k_{r_2}	1.0
$\mathcal{W}$	15,560 lb	k_{p0}	0.05	K_{p_v}	40.2
I_{xx}	3650 slug-ft^2	k_{p1}	−0.1	K_{p_h}	720
I_{yy}	80,000 slug-ft^2	k_{p2}	−1.0	K_{I_v}	10
I_{zz}	82,000 slug-ft^2	k_{q0}	−0.1	K_{I_h}	2.18
I_{xz}	490 slug-ft^2	k_{q1}	0.1	K_{D_v}	1030
k_{set}	0.2	k_{q2}	1.0	K_{D_h}	2970

With the benefit of hindsight and subsequent research, we revisit the events of 1967 by examining "how and what if" scenarios.

Aerodynamics

The aerodynamic forces and moments acting on the aircraft can be expressed in terms of the nondimensional force and moment coefficients through multiplication by a dimensionalizing factor and, in the case of the forces, a transformation from wind to body axes [48]. The forces and moments are therefore given by

$$\begin{bmatrix} X \\ Y \\ Z \end{bmatrix} = \bar{q}S \begin{bmatrix} \cos\alpha & 0 & -\sin\alpha \\ 0 & 1 & 0 \\ \sin\alpha & 0 & \cos\alpha \end{bmatrix} \begin{bmatrix} -C_{\mathrm{D}} \\ C_Y \\ -C_{\mathrm{L}} \end{bmatrix}, \tag{17}$$

$$\begin{bmatrix} L \\ M \\ N \end{bmatrix} = \bar{q}S \begin{bmatrix} b_{\mathrm{ref}} C_l \\ c_{\mathrm{ref}} C_m \\ b_{\mathrm{ref}} C_n \end{bmatrix}, \tag{18}$$

where $\bar{q}$ is the dynamic pressure; C_{L}, C_Y, and C_{D} are the lift, side-force, and drag coefficients respectively; and C_l, C_m, and C_n are the roll, pitch, and yaw moment coefficients. The values of the aircraft parameters such as the wingspan b_{ref}, the mean aerodynamic chord c_{ref}, and the wing surface area S are given in Table 1. The nondimensional force coefficients C_{L}, C_Y, C_{D}, and moment coefficients C_l, C_m, C_n, are functions of the control inputs as well as the aircraft state.

The X-15 has four main control inputs, the throttle δ_{th} to the XLR-99 rocket engine, the deflections δ_{f_1} and δ_{f_2} of the combined pitch/roll control surfaces (called elevons) on each wing, and the deflection δ_{r} of the large rudder. The X-15 is also equipped with speed brakes, which extend from the upper section of the rudder. Due to their position on the aircraft, these surfaces not only increase drag but also add a positive pitching moment. The speed brakes are modeled as the control input δ_{sb}, which can be either engaged or disengaged by the pilot but not by the onboard controller.

The elevon can be transformed into equivalent aileron and elevator deflections as

$$\delta_{\mathrm{e}} = \frac{\delta_{\mathrm{f}_1} + \delta_{\mathrm{f}_2}}{2}, \tag{19}$$

$$\delta_{\mathrm{a}} = \frac{\delta_{\mathrm{f}_1} - \delta_{\mathrm{f}_2}}{2}. \tag{20}$$

For control, it is convenient to work with δ_{e} and δ_{a} in place of δ_{f_1} and δ_{f_2}. We can now write the system control vector as

$$U_t = [\delta_{\mathrm{th}} \;\; \delta_{\mathrm{e}} \;\; \delta_{\mathrm{a}} \;\; \delta_{\mathrm{r}}]^T. \tag{21}$$

With the control inputs in (21), the force and moment coefficients in (17) and (18) are generated as

$$C_{\mathrm{L}} = C_{\mathrm{L}_{\mathrm{wb}}} + C_{\mathrm{L}_{\delta_{\mathrm{e}}}}\delta_{\mathrm{e}}, \tag{22}$$

$$C_{\mathrm{D}} = C_{\mathrm{D}_{\mathrm{wb}}} + C_{\mathrm{D}_{\delta_{\mathrm{e}}}}\delta_{\mathrm{e}} + C_{\mathrm{D}_{\delta_{\mathrm{sb}}}}\delta_{\mathrm{sb}}, \tag{23}$$

$$C_Y = C_{Y_\beta}\beta + C_{Y_p}p\frac{b_{\mathrm{ref}}}{2V_{\mathrm{T}}} + C_{Y_r}r\frac{b_{\mathrm{ref}}}{2V_{\mathrm{T}}} + C_{Y_{\dot\beta}}\dot\beta\frac{b_{\mathrm{ref}}}{2V_{\mathrm{T}}} + C_{Y_{\delta_{\mathrm{a}}}}\delta_{\mathrm{a}} + C_{Y_{\delta_{\mathrm{r}}}}\delta_{\mathrm{r}}, \tag{24}$$

$$C_l = C_{l_\beta}\beta + C_{l_p}p\frac{b_{\mathrm{ref}}}{2V_{\mathrm{T}}} + C_{l_r}r\frac{b_{\mathrm{ref}}}{2V_{\mathrm{T}}} + C_{l_{\dot\beta}}\dot\beta\frac{b_{\mathrm{ref}}}{2V_{\mathrm{T}}} + C_{l_{\delta_{\mathrm{a}}}}\delta_{\mathrm{a}} + C_{l_{\delta_{\mathrm{r}}}}\delta_{\mathrm{r}}, \tag{25}$$

$$C_m = C_{m_{\mathrm{wb}}} + C_{m_q}q\frac{c_{\mathrm{ref}}}{2V_{\mathrm{T}}} + C_{m_{\dot\alpha}}\dot\alpha\frac{c_{\mathrm{ref}}}{2V_{\mathrm{T}}} + C_{m_{\delta_{\mathrm{e}}}}\delta_{\mathrm{e}} + C_{m_{\delta_{\mathrm{sb}}}}\delta_{\mathrm{sb}}, \tag{26}$$

$$C_n = C_{n_\beta}\beta + C_{n_p}p\frac{b_{\mathrm{ref}}}{2V_{\mathrm{T}}} + C_{n_r}r\frac{b_{\mathrm{ref}}}{2V_{\mathrm{T}}} + C_{n_{\dot\beta}}\dot\beta\frac{b_{\mathrm{ref}}}{2V_{\mathrm{T}}} + C_{n_{\delta_{\mathrm{a}}}}\delta_{\mathrm{a}} + C_{n_{\delta_{\mathrm{r}}}}\delta_{\mathrm{r}}. \tag{27}$$

With the exception of $C_{\mathrm{L}_{\mathrm{wb}}}$, $C_{\mathrm{D}_{\mathrm{wb}}}$, and $C_{m_{\mathrm{wb}}}$, which are the contributions of the wing and body to the lift, drag, and pitching moment, respectively, each coefficient in (22)–(27) is a nondimensional derivative, where C_{y_x} denotes the derivative of C_y with respect to x. As the simulated X-15 moves through its flight envelope, these coefficients vary substantially with the angle of attack α as well as with the Mach number M. To capture this variation, lookup tables are used for each of the nondimensional coefficients as functions of M and α. The data for these tables are extracted from recorded flight data [49]–[51], wind tunnel measurements [51]–[53], and theoretical calculations [51], [53]. Equations (1)–(27) completely describe the open-loop dynamics of the simulated X-15.

Parametric uncertainty is included in the simulation model by adjusting the aircraft parameters in (1)–(9) and (17)–(18) as well as scaling the nondimensional coefficients in (22)–(27). One of the factors that caused the 1967 crash was an electrical disturbance that degraded the controls [39]. That is, the stick deflection produced less-than-expected control forces and moments, meaning the pilot had to move the stick farther to achieve the desired response. We can include this type of uncertainty in the model by scaling the nondimensional coefficients in (22)–(27) that precede the control surface deflections δ_{e}, δ_{a}, and δ_{r}. For example, a 60% loss of rudder effectiveness can be modeled by scaling $C_{Y_{\delta_{\mathrm{r}}}}$, $C_{l_{\delta_{\mathrm{r}}}}$, and $C_{n_{\delta_{\mathrm{r}}}}$ by 0.4. This uncertainty is equivalent to scaling the value of δ_{r}; the rudder

would have to move 2.5 times as far to generate the same forces and moments.

Actuators and Sensors

The aerodynamic control surface deflections on the X-15 aircraft are executed by hydraulic actuators. The dynamics of these actuators are modeled as second-order systems with transfer functions

$$G_{cs}(s) = \frac{\omega_n^2}{s^2 + 2\zeta\omega_n + \omega_n^2}, \tag{28}$$

where the damping ratio is $\zeta = 0.7$ and the natural frequency is $\omega_n = 90$ rad/s for the elevons and $\omega_n = 70$ rad/s for the rudder. The actuator deflection limits are taken to be $\pm 30^\circ$ for both the elevons and rudder.

As the X-15 climbs, the aerodynamic control surfaces become unable to provide controllability for the aircraft. Reaction controls in the form of small, monopropellant rockets are thus used to provide the necessary moments around each axis. These reaction controls are effective when the dynamic pressure decreases below 100 lb/ft^2 [54]. For the X-15 that level of dynamic pressure typically corresponds to altitudes greater than 125,000 ft. In this region, the actuator dynamics are modeled by the first-order system

$$G_{rc}(s) = \frac{1}{\tau_{rc} s + 1}, \tag{29}$$

with the time constant $\tau_{rc} = 1/34.6$ s [55].

During flight, the aircraft angular rates p, q, and r are measured by rate gyroscopes. The angle of attack α and the sideslip angle β are measured by a spherical flow-direction sensor. This sensor uses the differential pressure measurements from several pressure ports on a sphere mounted to the tip of the aircraft to determine the direction of the hypersonic flow. The dynamics of these sensors are neglected for simulation.

The simulation model does not include aerodynamic effects due to unsteady flow at the shear layer, vortex shedding, hypersonic shock, and turbulence. The contributions of these nonlinearities are ignored because of their small magnitude relative to the nonlinearities due to inertial, gravitational, and aerodynamic forces and moments. We ignore parameter variations in this model besides those due to loss of actuator effectiveness. Actuator nonlinearities due to hysteresis and rate saturation are also not included in the model. Although these nonlinearities were found to be problematic during re-entry, the anomalous behavior and the instability of the X-15-3 during the 1967 crash occurred during the climbing phase, and therefore the re-entry phase is not examined in this article. Another uncertainty not included in the model is flexible aircraft effects, such as structural modes and resulting vibrations, which may be a significant problem for hypersonic aircraft [28], [29], [56]. In fact, the X-15-3 required a notch filter in the control loop to avoid exciting structural resonances. However, unlike the saturation nonlinearity, excessive structural resonance was not known to cause instability and was not implicated in the 1967 crash [40], [41]. For these reasons, neither structural modes nor the notch filter are included in the model. Finally, "unknown unknowns" are not included in the model since their structure is not determinable. The purpose of delineating the known unknowns described above is to chip away the effects that are known to contribute to flight dynamics to minimize the remaining unmodeled effects. In summary, the goal of this section is not to determine an exact model of the X-15 but rather to create a tool that captures enough of the relevant dynamics with respect to the X-15-3 flight to make comparisons between the MH-96 and GMS-LS adaptive controllers.

The Feedback Controller

The control architecture is composed of an inner loop and a pilot model. The inner-loop controller operates on the quickly varying states, which evolve according to the aircraft longitudinal and lateral dynamics. The pilot model operates on the slowly varying states such as altitude and speed. The primary goal of the pilot model is to ensure that the aircraft follow the commanded altitude and speed profiles. The inner-loop controller is a reconstruction of the MH-96 adaptive controller [40]–[43], with three loops, one for each of the pitch, roll, and yaw axes. Figure 3(a) shows a block diagram of the pitch axis of the MH-96 [41], which is a slightly simplified representation of the MH-96 as equipped on the X-15-3. Figure 3(b) presents the block diagram of the reconstructed MH-96 controller.

A more detailed configuration of the MH-96 controller is given in [43]. The additional details addressed in [43] that are not shown in Figure 3 pertain to autopilot, fixed-gain, and reaction control blocks. The autopilot allowed the pilot to dial in desired values of α or θ. This feature is not part of the reconstructed MH-96 but is included in the pilot model. The fixed-gain loop was a fail-safe mode of operation that could be utilized in place of the adaptive system. This mode was not used during the 1967 crash and thus is not included in the simulation model. The reaction control system blends the transition from aerodynamic control surfaces to reaction controls at the edge of space. We assume that this blending is perfect, and thus the pilot retains control authority over the entire flight envelope.

The MH-96's target model of the X-15 is given by

$$G_m(s) = \frac{1}{\tau_m s + 1}, \tag{30}$$

where $\tau_m = 0.5$ s in the pitch axis and $\tau_m = 0.33$ s in the roll axis [40]. For the yaw axis, $G_m(s)$ is taken to be zero, that is, the model yaw rate $r_m \equiv 0$ rad/s. The error between the model angular rates p_m, q_m, and r_m and the measured rates

p, q, and r is fed back through the variable gains k_p, k_q, and k_r, respectively. The gain changes are initiated based on the amplitude of the limit cycle at the natural frequency of the servoactuator loop. A bandpass filter is used to isolate the oscillations at this frequency. The absolute value of the resulting bandpassed signal δ_{ad_f} is then compared to a constant setpoint k_{set} to obtain the gain computer input y defined by

$$y = k_{\mathrm{set}} - |\delta_{\mathrm{ad}_f}|, \tag{31}$$

where k_{set} is the threshold between acceptable and unacceptable oscillations.

To reproduce the behavior of the MH-96, an algorithm for adjusting the gains k_p, k_q, and k_r is determined so that the amplitude and rate of change of the gains are bounded above and below. The amplitude bounds, which ensure that structural feedback is minimized, are specified in [40] and [41]. The rate bounds are chosen such that the gains can be reduced rapidly from large values that might trigger instabilities and slowly increased so that the gains stay near critical values. The above considerations lead to the rule for adjusting k_q given by

$$\dot{k}_q = \begin{cases} 0, & \text{if } k_q \le k_{q_1} \text{ or } k_q \ge k_{q_2}, \\ k_{\mathrm{qd}_1}, & \text{if } k_{q_0} y \le k_{\mathrm{qd}_1}, \\ k_{\mathrm{qd}_2}, & \text{if } k_{q_0} y \ge k_{d_2}, \\ k_{q_0} y, & \text{otherwise}, \end{cases} \tag{32}$$

where k_{q_0} is the adaptation rate, k_{q_1} and k_{q_2} are the amplitude bounds, and k_{qd_1} and k_{qd_2} are the rate of change bounds. A similar rule is used to adjust k_p and k_r. The values of these constants, as well as corresponding constants for the roll and yaw loops, are given in Table 1.

Equation (32) ensures that, if the bandpassed control signals are smaller than the setpoint, then the gain computer increases the forward loop gain. Conversely, when the signals become large, signaling the onset of instability, the forward loop gain is decreased. Typical time profiles of these variable gains for the yaw loop are displayed in Figure 4(a) and (b), which show the time profiles for the MH-96 controller [40] along with the reconstructed MH-96 controller as shown in Figure 3(b), respectively. The gain adjustments for the pitch and roll loops behave similarly.

The pilot model is designed to operate on a slower time scale than the inner-loop controller. The inputs to the pilot model are $u = [V_{\mathrm{T}} \;\; h]^T$ as well as the commanded trajectory as a function of time

$$u_{\mathrm{cmd}}(t) = \begin{bmatrix} V_{\mathrm{T_{cmd}}}(t) \\ h_{\mathrm{cmd}}(t) \end{bmatrix}. \tag{33}$$

The commanded trajectory is extracted from [57] as a typical high-altitude mission. The output of the pilot model is the reference control signal $\delta_c = [\delta_{\mathrm{th}} \;\; \delta_{\mathrm{e}}]^T$. For these simulations the pilot is modeled as a proportional-integral-derivative controller with the transfer function

$$G_c(s) = K_{\mathrm{P}} + \frac{K_{\mathrm{I}}}{s} + \frac{K_{\mathrm{D}} s}{\frac{1}{N} s + 1}, \tag{34}$$

with $K_{\mathrm{P}} = \mathrm{diag}(K_{\mathrm{P_V}}, K_{\mathrm{P_h}})$, $K_{\mathrm{I}} = \mathrm{diag}(K_{\mathrm{I_V}}, K_{\mathrm{I_h}})$, and $K_{\mathrm{D}} = \mathrm{diag}(K_{\mathrm{D_V}}, K_{\mathrm{D_h}})$. The gains for both the speed and altitude loops are selected using the Ziegler-Nichols ultimate sensitivity method [58]. The pilot's role is therefore modeled in the simulation studies below as a servo for tracking in the

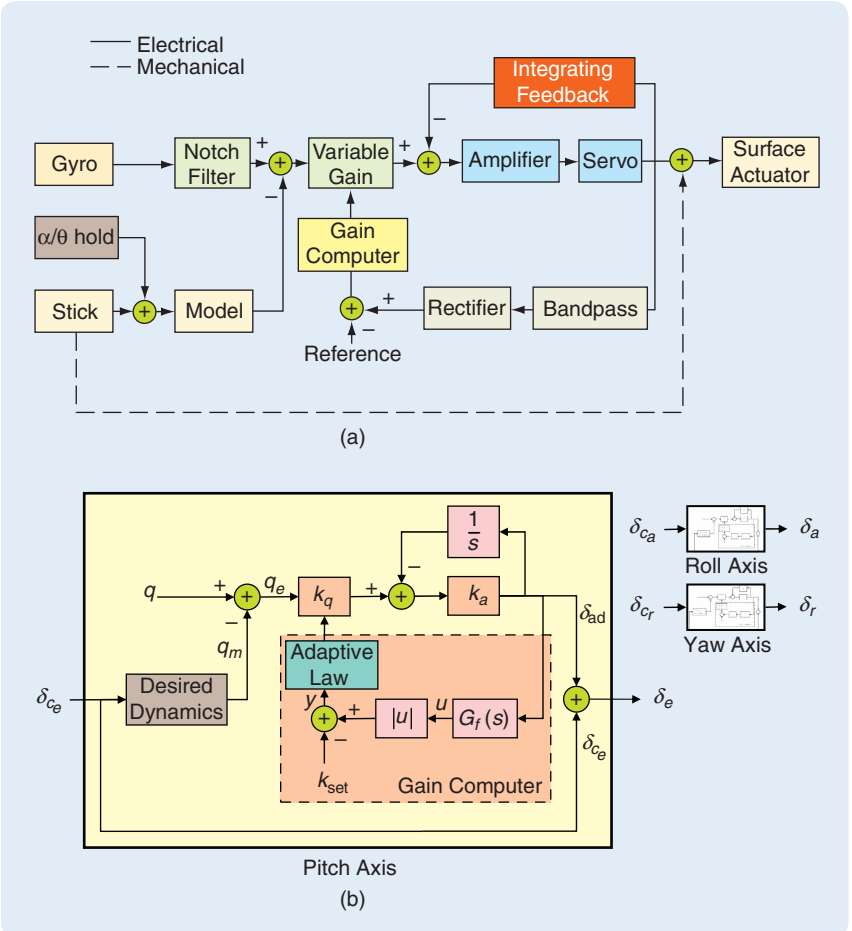

FIGURE 3 Schematic of the inner-loop control architecture. These block diagrams represent the pitch axis control of (a) the original MH-96 controller (reproduced from [41]) and (b) the reconstructed MH-96 controller. The control loops for roll and yaw have the same structure. The inner-loop controller used in the simulation captures all of the essential elements of the MH-96 inner-loop controller.

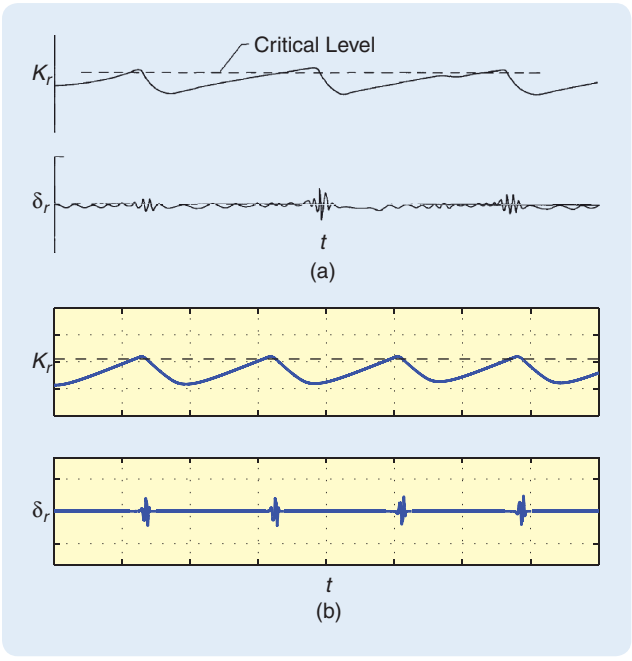

FIGURE 4 Gain changer operation. These plots display the typical gain changer performance and control surface activity for (a) the original MH-96 adaptive controller (reproduced from [40]) and (b) the reconstructed MH-96 controller. The gain changer increases the system gain until the critical level is reached, causing instability and oscillations in the control signal. When the oscillations become excessive, the system gain is reduced.

longitudinal states, whereas the failure mode during the 1967 crash, at least initially, involved a lateral instability that was not corrected. In a more complete examination of pilot-airplane interactions, such as [59], the pilot model could be constructed using the structure of the neuromuscular and central nervous system, and fit to empirical data [60], [61]. Such an exploration is beyond the scope of this article.

THE 1967 INCIDENT

With the X-15 simulation model and the reconstructed MH-96 controller in place, we now investigate the X-15-3 accident. Using the transcript of radio communication between the pilot and ground control [1], as well as limited flight data [44], the order of the events that occurred during the crash can be listed as follows:

i) At 85,000 ft, electrical disturbance slightly degrades control and the pilot switches to backup dampers.
ii) Planned wing rocking procedure is excessive.
iii) The X-15-3 begins a slow drift in heading.
iv) At the peak altitude, 266,000 ft, drift in heading pauses with airplane yawed 15° to the right of the desired heading.
v) Drift continues, and the plane begins descending at a right angle to the flight path.
vi) The X-15-3 enters a spin.
vii) At 118,000 ft, the pilot recovers from the spin and enters inverted Mach-4.7 dive.
viii) The MH-96 begins a limit cycle oscillation in pitch, preventing further recovery techniques.
ix) The X-15-3 experiences 15 g's vertically, 8 g's laterally, and the aircraft breaks apart.

Equations (1)–(27), which describe the X-15 dynamics, and the multiloop control architecture with the adaptive algorithm in (32) are simulated to represent the overall flight control system and the flight dynamics of the X-15-3. Table 1 lists all of the parameter values that are used. The pilot is assumed to engage the speed brakes during the final stages of the descent, that is,

$$\delta_{sb} = \begin{cases} 1, & \text{if } 350 \le t \le 400, \\ 0, & \text{otherwise.} \end{cases} \tag{35}$$

The system is simulated for a nominal set of conditions, and the tracking performance is shown in Figure 5(a)–(d). The altitude tracking error is less than 1% of the maximum altitude, and the speed tracking error is less than 3% of the maximum speed. This performance corresponds to a successful high-altitude mission.

We now attempt to recreate the conditions of the 1967 crash. The failure mode during that flight was a combination of the loss of control effectiveness caused by the electrical disturbance and pilot distraction, confusion, and possible vertigo [39]. We do not attempt to model the pilot's actions during this high-stress event. Instead, we aim to determine a possible set of control failures, which, when included in the simulation model, display the anomalous behavior described in events ii)–ix). The drift in heading, event iii), suggests that some asymmetry had arisen in the controls. We found that including the scaling factor of 0.2 on the signal δ_{f_1} in the simulated X-15-3 produced the instability described by events iii)–vi). This situation corresponds to an 80% loss of control effectiveness in the right elevon.

As shown in Figure 6, the tracking performance begins to degrade soon after the failure at $t = 80$ s. It is not until approximately 120 s later, as the simulated X-15-3 nears its peak altitude, that the aircraft makes a dramatic departure from the commanded trajectory. The simulation is stopped at $t = 385$ s when the altitude reaches 0 ft; however, the accuracy of the model most likely breaks down earlier, perhaps soon after the dive is initiated at a time between $t = 250$ s and $t = 300$ s.

Examination of the aircraft states reveals additional similarities between the simulation and events i)–ix). The first of these similarities is event iii), a steady drift in heading angle ψ, which can be attributed to the asymmetry of the control failure. Figure 7(a) shows that this drift is initiated at the onset of the disturbance and that the drift oscillates around 15° between $t = 120$ s and $t = 200$ s as described in event iv). This drift is followed by a rapid downward spiral as shown in Figure 7(b) for $t = 180$ s and onward. We also observe event viii), the undamped oscillation in the limit

cycle amplitude, which prevents the adaptive controller from reducing the variable gain on the pitch axis (see Figure 8). It was therefore difficult or impossible for the pilot to pitch up the aircraft and recover from the dive. Lastly, we see the large accelerations in both the lateral and vertical directions (see Figure 9), which ultimately caused the X-15-3 to break apart, corresponding to event ix).

Some of the events reported in [1] are not reproduced. For example, the planned wing rocking maneuver in event ii) is not excessive in the simulation. The most likely reason for this discrepancy is that the pilot's commands were excessive, as suggested in [39], due to the pilot's increased workload or vertigo. Additionally, figures 6(a) and 7 show that the aircraft does not recover from the spin as described in event vii). This difference is most likely due to the fact that the pilot employed spin recovery techniques that are beyond the scope and capability of the pilot model described in (34). With the exception of these two events, all the events i)–ix) of the crash are observed in the simulation.

In summary, a sudden change in actuator effectiveness, which could have been caused by the electrical disturbance, causes the dynamics to depart significantly from those represented in the model and therefore in the control design. As a result, the control gain choices, despite the flexibility provided by the adaptive feature, are inadequate, causing the overall control system to be unable to recover from the onset of instability leading up to the crash.

LYAPUNOV-STABILITY-BASED ADAPTIVE CONTROLLER

The Lyapunov-based controller used in the following simulation studies is adaptive; explicitly compensates for parametric uncertainties, actuator dynamics, and actuator saturation; and, like all controllers, implicitly accommodates

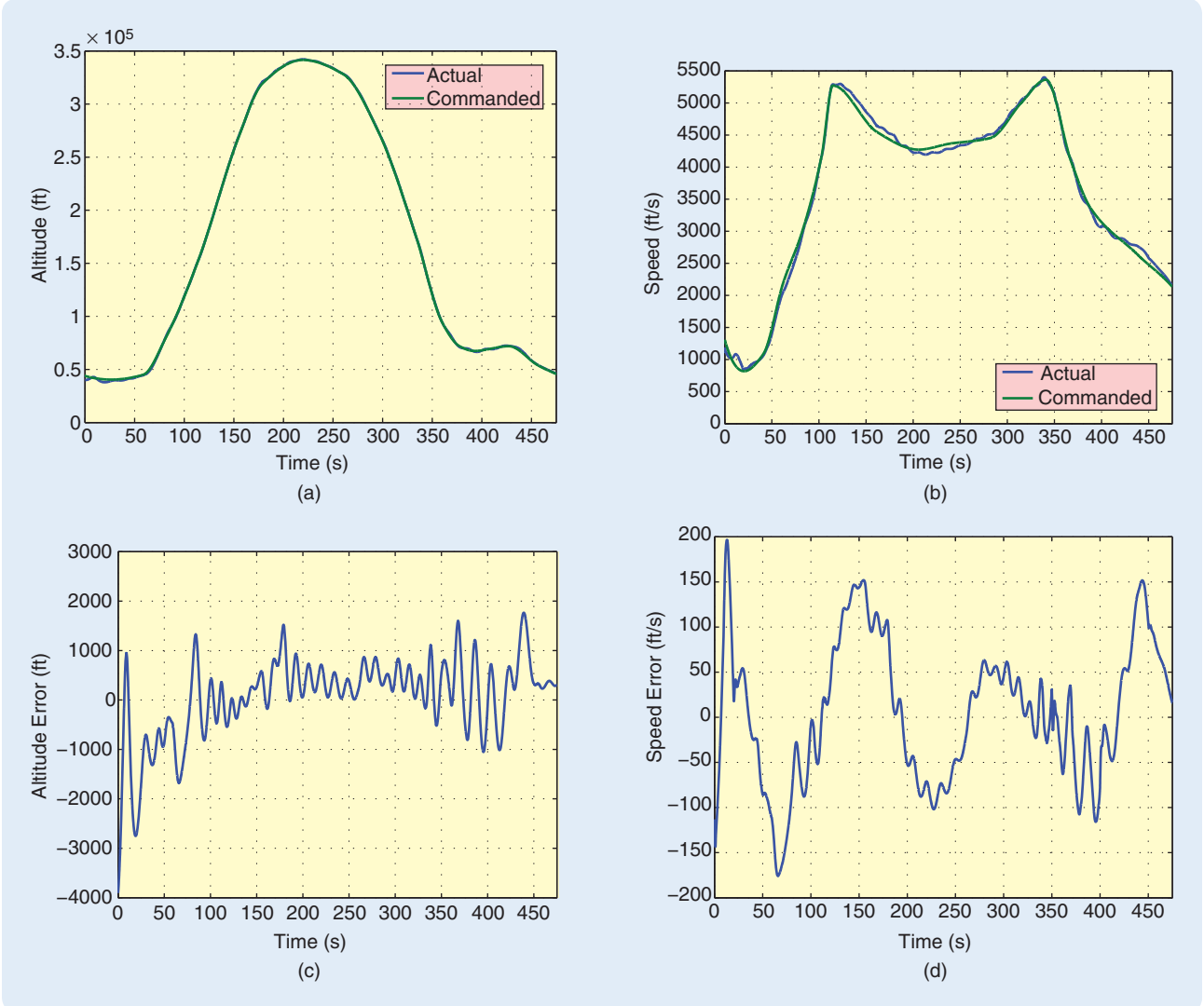

FIGURE 5 Tracking performance of the simulated X-15-3 with the reconstructed MH-96 controller in the nominal case. The altitude error is less than 1% of the maximum altitude achieved. The speed error is less than 3% of the maximum speed. The reconstructed MH-96 can stabilize the aircraft and complete maneuvers that are comparable to the original controller. (a) Altitude, (b) speed, (c) altitude error, and (d) speed error.

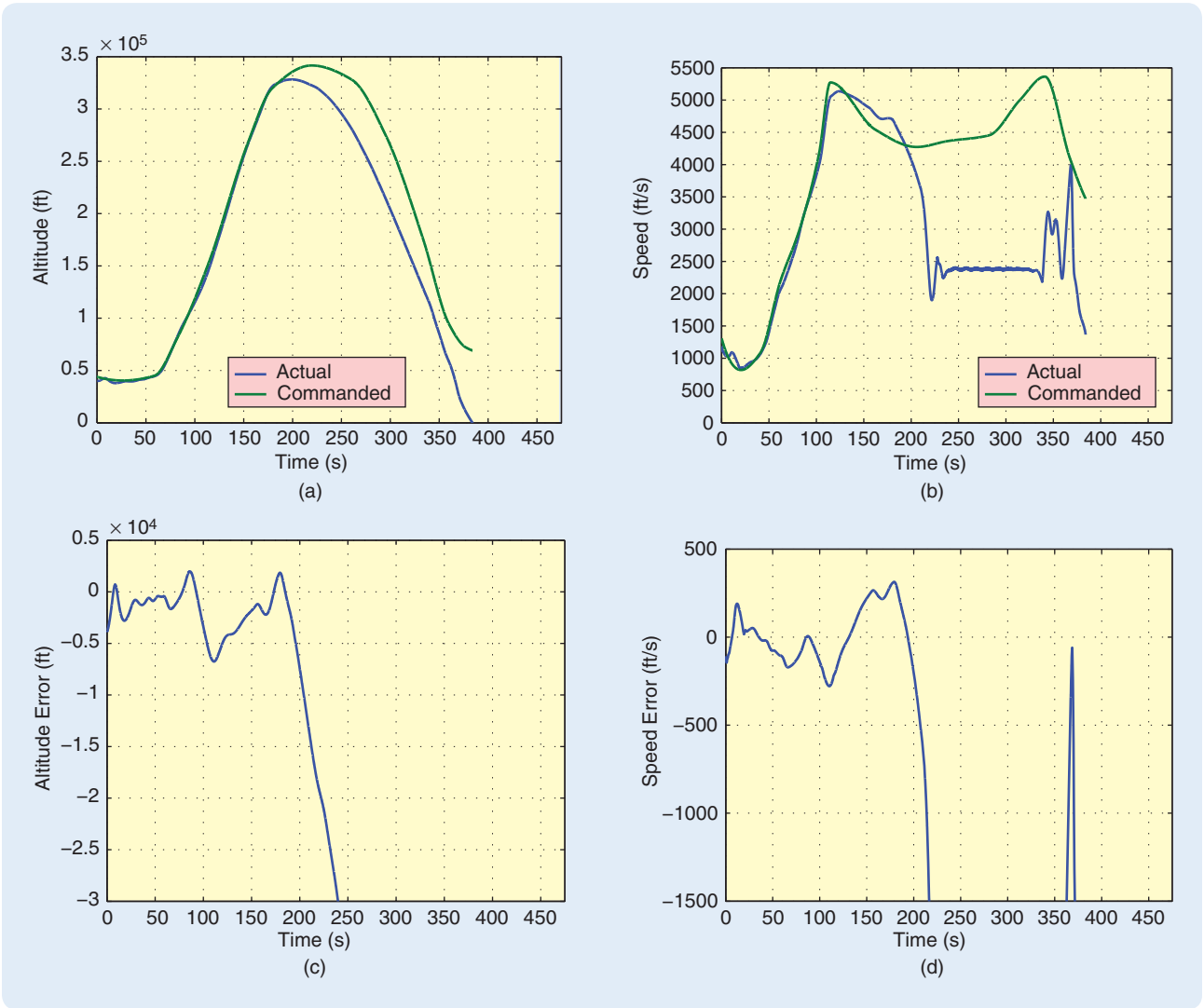

FIGURE 6 Tracking performance of the simulated X-15-3 with the reconstructed MH-96 controller in the failure case. An 80% loss of control effectiveness of the right elevon occurs at $t = 80$ s. Initially the altitude and speed tracking performance degrades only slightly, with tracking errors remaining below 1% and 6%, respectively. However, the system departs dramatically from the commanded trajectory at $t = 200$ s. According to [1], the actual X-15 began its dive between $t = 180$ s and $t = 210$ s. (a) Altitude, (b) speed, (c) altitude error, and (d) speed error.

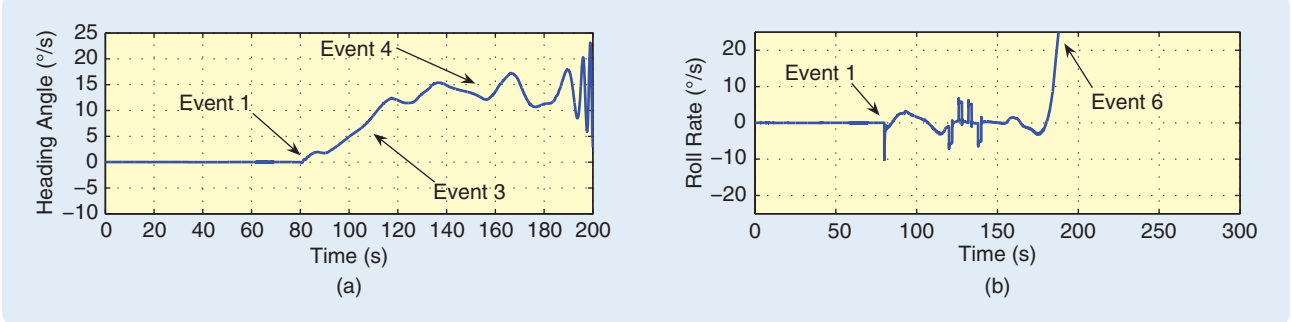

FIGURE 7 Simulated X-15-3 heading angle ψ and roll rate r. (a) shows a slow drift in heading, which briefly halts at around 15° as the simulated X-15-3 reaches its peak altitude. (b) shows that the roll rate becomes excessive as the simulated X-15-3 enters the dive, corresponding to a rapid spin. Of the events i)–ix) that occurred during the crash in 1967, seven of those are reproduced in the simulation studies.

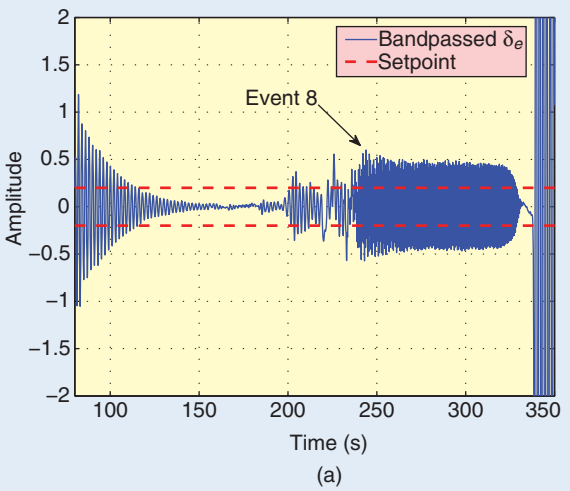

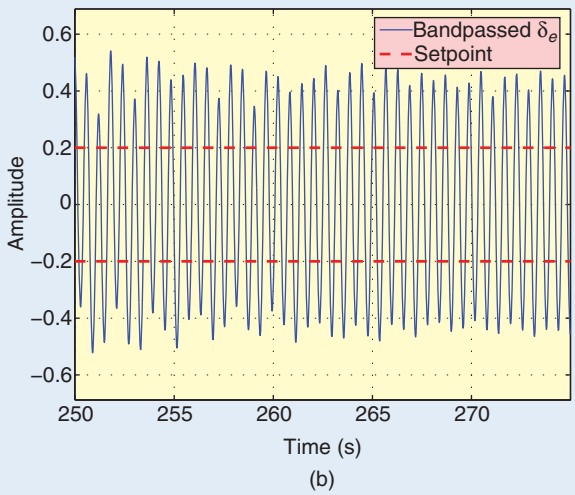

FIGURE 8 Limit cycles in the reconstructed MH-96 pitch gain loop. (a) shows the input to the adaptive gain computer over time. The forward loop gain is reduced when this input signal becomes larger than the setpoint. (b) displays a blowup of the signal between $t = 250$ s and $t = 275$ s, showing the existence of undamped oscillations, which prevent the gain changer from correctly adjusting the gain.

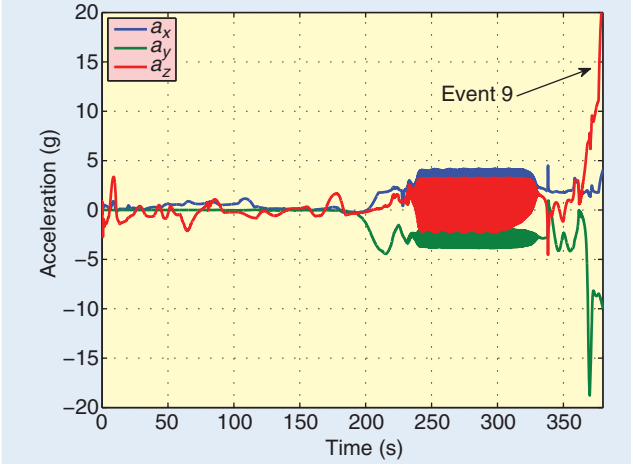

FIGURE 9 Accelerations experienced by the simulated X-15-3 in the failure case. a_x, a_y, and a_z represent acceleration in the body-fixed x-, y-, and z-axes, respectively. This plot shows the excessive acceleration experienced by the simulated X-15-3. As reported in [1], the aircraft experienced around 8 g's laterally and 15 g's vertically before breaking apart.

some amount of unmodeled dynamics, time delays, nonlinearities, and additional "unknown unknowns" [2], [3], [14], [16]–[21], [30].

In the following simulation studies, the reconstructed MH-96 controller is replaced with the GMS-LS adaptive controller, and the same maneuver is simulated. The overall block diagram of the GMS-LS adaptive control architecture is shown in Figure 10. This architecture consists of a baseline inner-loop controller, which is augmented with an inner-loop adaptive controller to compensate for the fast states, as well as the pilot model described by (34) to control the slow states of airspeed and altitude. The inner-loop baseline and adaptive controllers are discussed in more detail below.

Inner-Loop Adaptive Controller Design

The GMS-LS adaptive controller accommodates coupling between states, actuator saturation, and parametric uncertainties. In addition to the angular rate feedback used by the MH-96 controller, this architecture uses feedback of the alpha and beta states measured by the spherical flow-direction sensor, integral action, baseline control action, and online adjustment of several parameters. While the MH-96 controller has three variable gains, one for each axis, the GMS-LS adaptive controller has 21 adaptive parameters corresponding to all combinations of states and axes. The procedure for designing the baseline and adaptive control components is discussed in this section. An examination of the performance of this controller and its ability to guarantee stable behavior in the presence of actuator uncertainties is also discussed here.

Baseline Controller

The baseline controller is a linear-quadratic-regulator (LQR) full-state-feedback controller that includes integral action on the fast aircraft states. A schedule of LQ gain matrices is designed by linearizing the flight dynamics

$$\dot{X}_t = f_p(X_t, U_t), \tag{36}$$

at multiple trim points (X_{t_i}, U_{t_i}) selected to sample the flight regime of interest.

Although the X-15-3 measures all the fast states $X_f = [\alpha \ \beta \ p \ q \ r]^T$, only the roll, pitch, and yaw rates p, q, and r are fed back by the MH-96 controller. The GMS-LS adaptive controller uses feedback of α and β in addition to

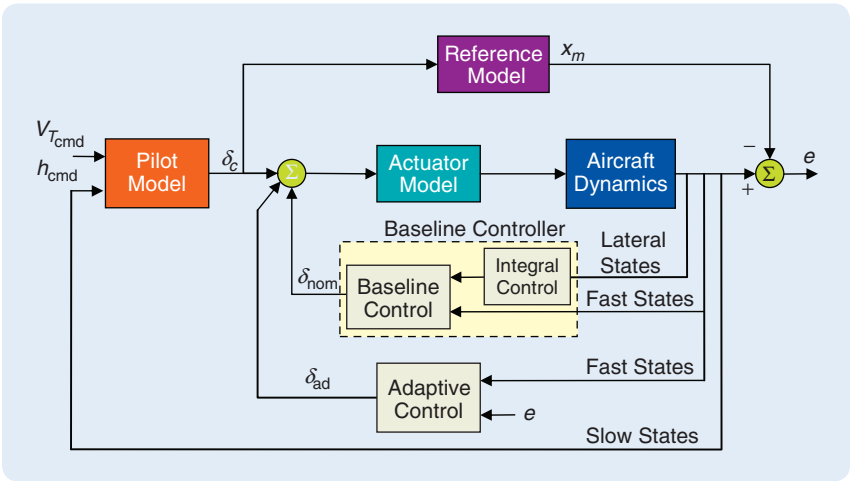

FIGURE 10 Overall control structure of the gain-scheduled, magnitude-saturation-accommodating, Lyapunov-stability-based (GMS-LS) adaptive controller. The baseline controller (composed of the baseline control and integral control subsystems) is augmented by the adaptive control. The adaptive controller operates on the error between the aircraft plant and the reference model. Both the adaptive and baseline controllers operate on the fast longitudinal and lateral states, while the pilot model operates on only the slow states.

p, q, and r. The fast states X_f and the corresponding control inputs $U_f = [\delta_e \ \delta_a \ \delta_r]^T$ can be extracted from the state vector X_t and the control vector U_t leading to the linearized flight dynamics

$$\dot{x}_p = A_{p_i} x_p + B_{p_i} \delta + d_{p_i}, \tag{37}$$

where

$$A_{p_i} = \left.\frac{\partial \dot{X}_f}{\partial X_f}\right|_{X_{f_i}, U_{f_i}}, \qquad B_{p_i} = \left.\frac{\partial \dot{X}_f}{\partial U_f}\right|_{X_{f_i}, U_{f_i}}, \tag{38}$$

$x_p = X_f - X_{f_i} \in \Re^n$, $\delta = U_f - U_{f_i} \in \Re^m$, and $d_{p_i} \in \Re$ is a constant trim disturbance. The baseline controller is designed using the parameters given by (38).

To overcome the drift in the lateral dynamics due to the trim disturbance, an integral controller is added for the system controlled output y_p given as

$$y_p = C_p x_p = [p \ \ r]. \tag{39}$$

We then write the integral error state x_c as

$$x_c(t) = \int_0^t [y_p(\tau) - y_{cmd}(\tau)] d\tau, \tag{40}$$

where $y_{cmd}(t)$ is a bounded, time-varying reference command. With the exception of the wing-rocking maneuver described in event ii), the reference command corresponding to the 1967 flight is $y_{cmd}(t) = [0 \ \ 0]$. That is, the lateral control problem is a regulation problem. We write the dynamics of the integral error state as

$$\dot{x}_c = A_c x_c + B_c x_p. \tag{41}$$

The nominal baseline LQ controller is then designed in the form

$$\delta_{nom} = K_{x_i} x, \tag{42}$$

where $x = [x_p^T \ x_c^T]^T$, and K_{x_i} denotes the nominal feedback gain matrix designed for the dynamics given by (37) and (41) around the ith trim point and chosen to minimize the cost function

$$J = \int_0^\infty (x^T Q_{lqr} x + \delta_{nom}^T R_{lqr} \delta_{nom}) dt. \tag{43}$$

The matrix Q_{lqr} is diagonal with diagonal entries [10 10 100 5000 100 10 10] and $R_{lqr} = I_3$. A schedule of nominal LQ gain matrices is thus constructed for the baseline controller.

Adaptive Controller

The goal of the adaptive controller is to accommodate uncertainties that occur due to actuator anomalies. A parametric uncertainty matrix Λ, which represents loss of control effectiveness, and a known saturation nonlinearity are incorporated in the linearized dynamics (37) as

$$\dot{x}_p = A_{p_i} x_p + B_{p_i} \Lambda \text{sat}(\delta) + d_{p_i}, \tag{44}$$

where the saturation function $\text{sat}(\delta)$ is defined componentwise for each component of δ as

$$\text{sat}(\delta_j) = \begin{cases} \delta_j & \text{if } |\delta_j| \le \delta_{j_{max}}, \\ \delta_{j_{max}} \text{sgn}(\delta_j) & \text{if } |\delta_j| > \delta_{j_{max}}, \end{cases} \tag{45}$$

where δ_j is the jth component of δ and $\delta_{j_{max}}$ are the known input saturation limits. The augmented plant dynamics are therefore given by

$$\begin{bmatrix} \dot{x}_p \\ \dot{x}_c \end{bmatrix} = \begin{bmatrix} A_{p_i} & 0 \\ B_c & A_c \end{bmatrix} \begin{bmatrix} x_p \\ x_c \end{bmatrix} + \begin{bmatrix} B_{p_i} \\ 0 \end{bmatrix} \Lambda \text{sat}(\delta) + \begin{bmatrix} d_{p_i} \\ 0 \end{bmatrix}, \tag{46}$$

or, equivalently,

$$\dot{x} = A_i x + B_i \Lambda u + d_i, \tag{47}$$

where $u = \text{sat}(\delta)$. The overall dynamics given by (47) are used for the adaptive control design.

To ensure safe adaptation, target dynamics are specified for the adaptive controller using a reference model. This model is selected using the baseline controller and the plant dynamics with no actuator uncertainties. Thus, the main goal of the adaptive controller is to recover and maintain

baseline closed-loop system performance in the presence of the uncertainty modeled by Λ. The reference model is defined as

$$\dot{x}_{\text{ref}} = (A_i + B_i K_{x_i}) x_{\text{ref}} + B_i \delta_c = A_{\text{ref}_i} x_{\text{ref}} + B_{\text{ref}_i} \delta_c. \quad (48)$$

Using (47) and (48), an adaptive control input is generated as

$$\delta_{\text{ad}} = \theta_x^T(t) x + \theta_d(t) = \Theta^T(t) \omega(t), \quad (49)$$

where $\Theta^T = [\theta_x^T \ \theta_d^T]$ are adaptive parameters that are adjusted in the adaptive laws given in (50)–(51) and the linear regressor is $\omega = [x^T \ 1]^T$.

The error e between the state of the plant and that of the reference model might be the result of several factors, including parametric uncertainties and the effects of actuator saturation. However, by exploiting explicit knowledge of the actuator saturation limits, we can calculate the error e_Δ due to saturation and instead adapt only to the augmented error $e_u = e - e_\Delta$. This approach provides guaranteed stability in the presence of actuator saturation limits while enforcing a bound on the adaptive parameters Θ, as shown in [5]. The adaptive laws are given by

$$\dot{\Theta} = \Gamma_i \text{Proj}(\Theta, -\omega e_u^T P_i B_{p_i}), \quad (50)$$

$$\dot{\hat{\Lambda}} = -\Gamma_{\Lambda_i} \text{diag}(\Delta u) B_{pi}^T P_i e_u, \quad (51)$$

where $\Delta u = \delta - \text{sat}(\delta)$ and P_i is the solution to the Lyapunov equation

$$A_{\text{ref}_i}^T P_i + P_i A_{\text{ref}_i} = -Q, \quad (52)$$

where Q is a positive-definite matrix. The projection operator $\text{Proj}(\Theta, y)$ is defined as

$$\text{Proj}(\Theta, y) = \begin{cases} y - \dfrac{\nabla f(\Theta)(\nabla f(\Theta))^T}{\|\nabla f(\Theta)\|^2} y f(\Theta), & \text{if } f(\Theta) > 0 \text{ and } y^T \nabla f(\Theta) > 0, \\ y, & \text{otherwise,} \end{cases} \quad (53)$$

where $f(\Theta)$ is defined columnwise for the jth column as

$$f(\Theta_j) = \frac{\|\Theta_j\|^2 - \Theta_{\max}^2}{\epsilon \Theta_{\max}^2}, \quad (54)$$

where $\Theta_{\max}$ is the desired upper bound on Θ and $\epsilon > 0$ is the projection tolerance. The adaptive gains at the ith trim point Γ_i are selected according to the empirical formula described in [6].

The structure and formulation of the adaptive laws is based on Lyapunov stability theory; the adaptive laws given in (50)–(51) are such that the derivative of the Lyapunov function is negative definite outside a compact set. The use of the projection operator in (50) guarantees stability and robustness [2], [3]. The details of the stability proof can be found in [30]. The inner-loop control input is a combination of the inputs from the pilot model δ_c, the baseline controller δ_{nom}, and the adaptive controller δ_{ad}, that is,

$$\delta = \delta_c + \delta_{\text{nom}} + \delta_{\text{ad}}. \quad (55)$$

The overall control architecture is shown in Figure 10.

Simulation Results

The first step in the simulation study is to select a sufficient number of trim points (X_{f_i}, U_{f_i}) to cover the commanded trajectory, which is a path in the space of altitude and speed. The trim points are distributed uniformly across this path as shown in Figure 11.

The next step is to simulate the GMS-LS adaptive inner-loop controller described in (49)–(55) with the simulated X-15 model and pilot model in (34). The speed brakes are engaged as described in (35). The initial conditions for the simulation are given by (X_{f_1}, U_{f_1}), that is, the aircraft is initially trimmed at the first trim point.

In the nominal case where no failures are present $(\Lambda = I_3)$, the aircraft is commanded to track the trajectory given by (33), and the resulting performance is shown in Figure 12(a)–(b). Figure 12(c)–(d) shows that the errors are less than 1% of the maximum in the case of altitude and less than 3% of the maximum in the case of speed. This level of performance is similar to that of the reconstructed MH-96 adaptive controller in the case where no failures are present. This achievement is a testament to the skill of the MH-96 control designers.

However, the performance of the two controllers in the failure case with 80% loss of control effectiveness in the

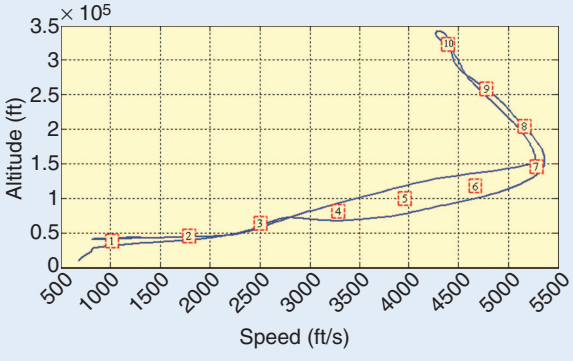

FIGURE 11 The commanded trajectory in altitude-speed space. This plot shows the commanded path for the simulated X-15-3 along with labels of the locations of the trim points used for controller design. Ten trim points are used to estimate the evolution of the parameters.

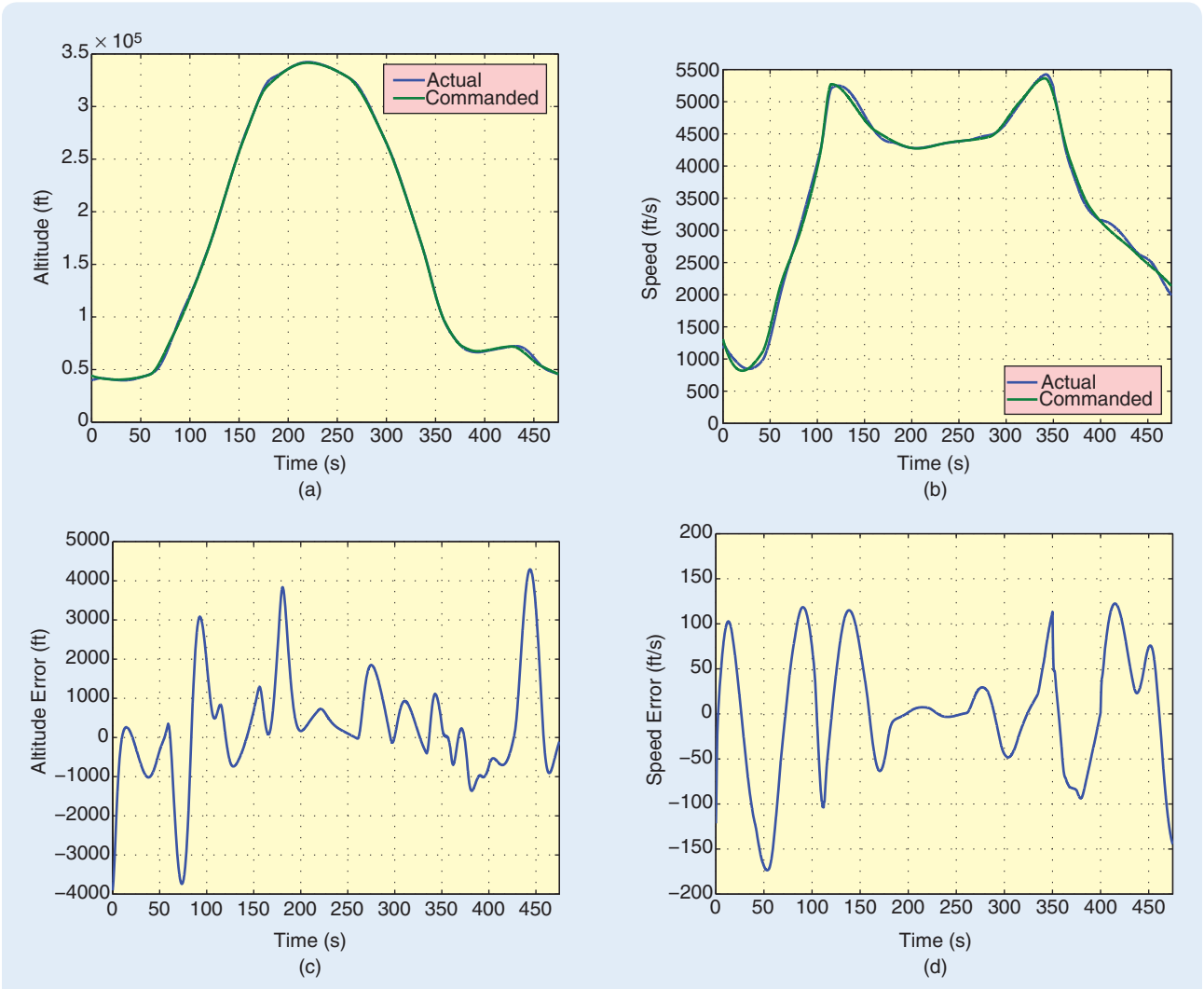

FIGURE 12 Tracking performance of the simulated X-15-3 with the gain-scheduled, magnitude-saturation-accommodating, Lyapunov-stability-based (GMS-LS) adaptive controller in the nominal case. The altitude error is less than 1% of the maximum altitude achieved. The speed error is less than 3% of the maximum speed. These plots show that the GMS-LS adaptive controller can stabilize the aircraft and complete a typical maneuver. The tracking performance of the GMS-LS adaptive controller is comparable to that of the reconstructed MH-96 controller. (a) Altitude, (b) speed, (c) altitude error, and (d) speed error.

right elevon is quite different. Figure 13 shows that not only does the GMS-LS adaptive controller maintain stability, but the performance in the failure case is comparable to that of the nominal case. That is, the desired performance of the GMS-LS adaptive controller is retained despite the parametric uncertainty. The adaptive controller accomplishes this level of performance while at or near the actuator limits for significant periods of time as can be seen in Figure 14.

The observations show that the GMS-LS adaptive controller is more effective than the reconstructed MH-96 at maintaining stability in spite of this severe actuator uncertainty for this maneuver. To determine whether this robustness is a result of the LQR inner-loop controller or of the adaptive augmentation, the same simulation is repeated with adaptation turned off. In this case, the GMS-LS adaptive architecture reduces to a gain-scheduled LQR proportional-integral (PI) controller. With adaptation off, the aircraft is not able to complete the maneuver successfully in the failure case.

We now investigate how the increased robustness is related to features of the GMS-LS adaptive controller. We thus reduce the complexity of the GMS-LS controller in several stages so that, at the final stage, the GMS-LS architecture is equivalent to the reconstructed MH-96 controller. These intermediate stages bridge the gap between the two controllers to highlight the features that set the two apart. At each stage the corresponding closed-loop system is simulated for the failure case demonstrated in figures 6–9, 13, and 14. The resulting RMS velocity and altitude tracking errors are calculated from $t = 0$ until the simulation is

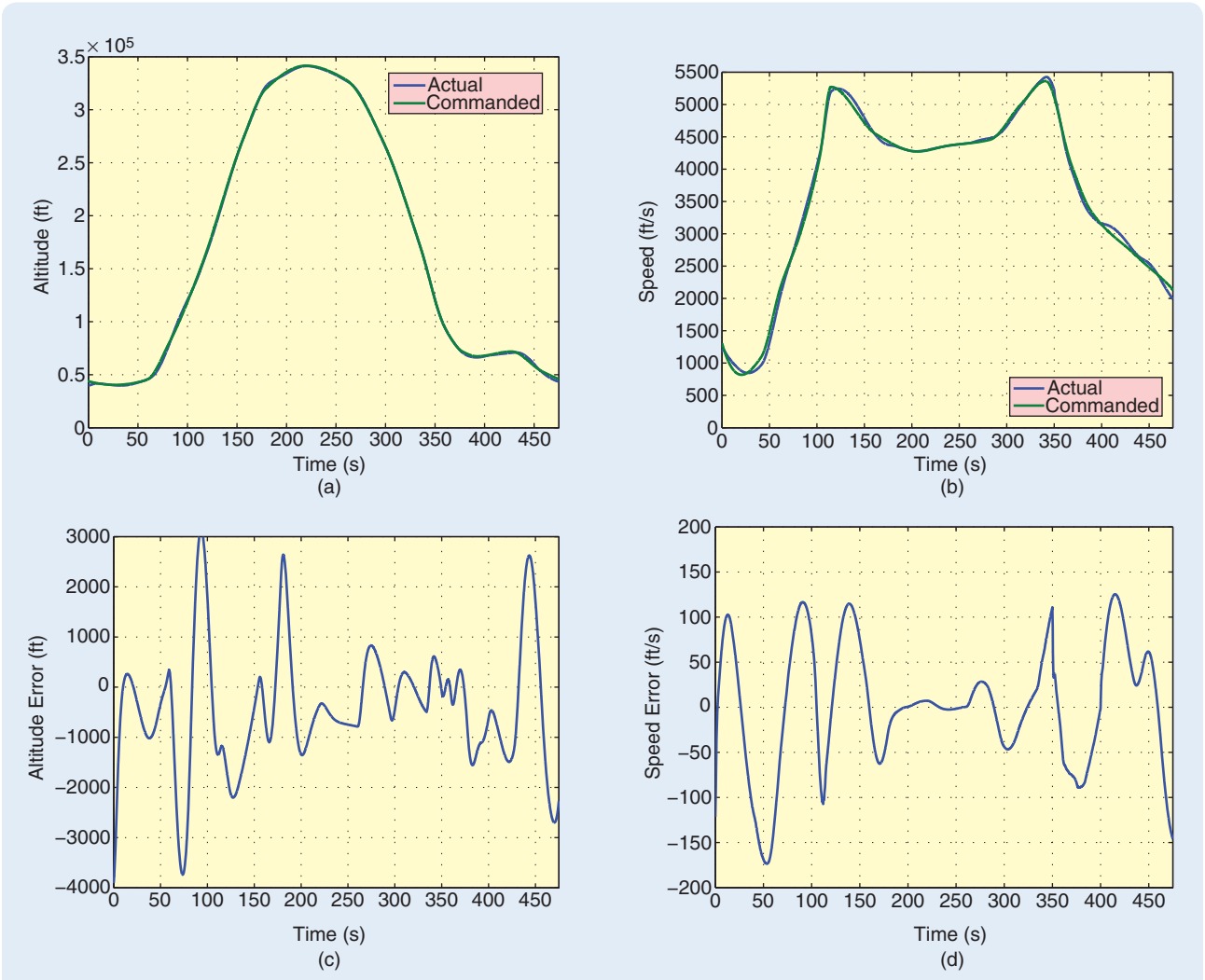

FIGURE 13 Tracking performance of the simulated X-15-3 with the gain-scheduled, magnitude-saturation-accommodating, Lyapunov-stability-based adaptive controller in the failure case. An 80% loss of control effectiveness is applied to the right elevon at $t = 80$ s. However, the adaptive controller maintains stability despite this failure. Moreover, the performance in the failure case is comparable to that of the nominal case. (a) Altitude, (b) speed, (c) altitude error, and (d) speed error.

stopped or the maneuver is completed. These errors are presented in Table 2.

In stage 1 we eliminate the coupling between various states by replacing θ_x in (49) by θ_x'. The matrix θ_x' retains only the entries of θ_x that correspond to the dominant coupling between the states and control inputs. Figure 15(a) shows which parameters are removed. The corresponding entries of the baseline feedback gain matrix K_{x_i} are removed as well. This parameter removal process is equivalent to removing adaptive control loops. The resulting controller no longer has the same stability guarantees as the GMS-LS adaptive controller.

Since the MH-96 controller does not feed back α, β, and integral error states, in stage 2 we remove these control loops from the GMS-LS controller. The associated entries of θ_x and K_{x_i} are removed as well, as shown in Figure 15(b). The total number of adaptive parameters in this stage is three, which is the same number of parameters as in the MH-96.

In stage 3, the error e_u in the adaptive laws (50)–(51) is changed to e, which corresponds to the case where the GMS-LS adaptive controller ignores the fact that the actuator can saturate. For stages 1–3 the GMS-LS adaptive controller can complete the maneuver successfully, resulting in low velocity and altitude tracking errors, as shown in Table 2.

In the final stage, the adaptive laws (50)–(51) are replaced by those of the reconstructed MH-96 given in (32), making it identical to the reconstructed MH-96 adaptive controller. As expected, this controller fails as observed in Figure 6. As an additional test, the reconstructed MH-96 is modified by adding the saturation-accommodating feature of the

TABLE 2 Tracking performance in the failure case. The root mean square of the tracking error is calculated for the gain-scheduled, magnitude-saturation-accommodating, Lyapunov-stability-based (GMS-LS) adaptive controller with adaptation on (GMS-LS) and off [linear quadratic regulator (LQR PI)], several intermediate controllers, the reconstructed MH-96 controller, and the reconstructed MH-96 controller with the augmented error modification, denoted MH-96+. The tracking errors are high for the LQR PI controller, the reconstructed MH-96 controller, and the reconstructed MH-96+ since they all lose stability in the failure case. This table also shows that removing some adaptive parameters in the failure case can improve tracking performance.

	GMS-LS	LQR PI	Stage 1	Stage 2	Stage 3	MH-96	MH-96+
RMS V_T error (ft/s)	59.6	767	50.2	50.5	51.3	1029	1244
RMS H error (ft)	2785	80,180	1065	1051	946.0	21,860	17,469

GMS-LS adaptive controller. This modification, however, is insufficient, and the simulated X-15-3 continues to exhibit the instability and eventual crash, as shown in Table 2 under the heading MH-96$^+$.

The results of this dissection show that i) augmenting the reconstructed MH-96 controller with the saturation-accommodating feature does not suffice, and ii) the modification that results in successful completion of the maneuver is the replacement of the gain update laws. It is interesting to note that slightly improved tracking performance is obtained with the simplified versions of the GMS-LS adaptive controller compared to the performance of the full version. The reason for the improved performance might be that the particular failure we examine in this study does not introduce any unexpected coupling between states. Thus, the simplified versions, which do not account for this coupling, can maintain stability and complete the maneuver. It remains to be shown that any uncertainties that exacerbate this coupling could result in a diminished robustness and therefore larger tracking errors.

DISCUSSION AND CONCLUSIONS

Simulation results show that a model of the X-15 aircraft and the MH-96 controller performs satisfactorily under nominal conditions. However, when subjected to a severe disturbance, the system fails, displaying much of the anomalous behavior observed during the crash of the X-15-3 in 1967. When the reconstructed MH-96 controller is replaced by the GMS-LS adaptive controller, the simulated X-15-3 not only achieves high performance in the nominal case but also exhibits increased robustness to uncertainties. Indeed, when subjected to the same failure, the GMS-LS adaptive controller maintains both stability and much of its performance, completing the simulated maneuver safely. The main feature of the GMS-LS adaptive controller that contributes to this dramatic difference appears to be its Lyapunov-stability-based adaptive law for adjusting the control parameters.

It is certainly possible that, under an alternative set of flight conditions, one or more of the effects not included in the model might become significant. In such a case, a

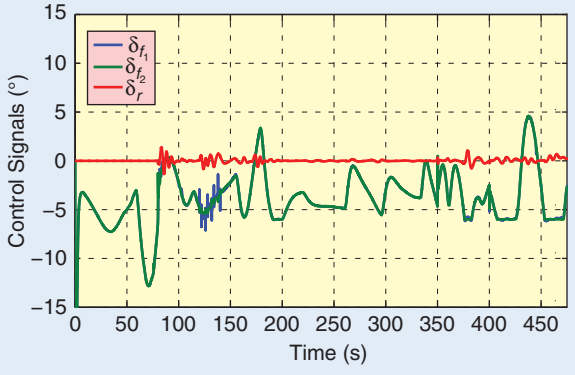

FIGURE 14 Control inputs for the maneuver in Figure 13. Note that while the left actuator's limit is at the nominal value of $\pm 30^\circ$, the right actuator's limit is actually $\pm 6^\circ$ due to the 80% loss of control effectiveness. The small oscillations between $t = 120$ s and $t = 140$ s correspond to the commanded wing-rocking procedure. The gain-scheduled, magnitude-saturation-accommodating, Lyapunov-stability-based (GMS-LS) adaptive controller does not ask for more control authority than the reconstructed MH-96 controller but rather uses the available control authority more effectively. The GMS-LS adaptive controller thus maintains stability near the saturation limits.

	δ_e	δ_a	δ_r
α	θ_{11}	×	×
β	×	×	×
p	×	θ_{32}	×
q	θ_{41}	×	×
r	×	×	θ_{53}
p_I	×	θ_{62}	×
r_I	×	×	θ_{73}

(a)

	δ_e	δ_a	δ_r
α	×	×	×
β	×	×	×
p	×	θ_{32}	×
q	θ_{41}	×	×
r	×	×	θ_{53}
p_I	×	×	×
r_I	×	×	×

(b)

FIGURE 15 Adaptive parameters in (a) stage 1 and (b) stage 2. Here the × in the ith row and jth column represents adaptive parameters that are dropped, removing the control loop from the ith state to the jth control input, whereas θ_{ij} represents parameters that are kept in each stage. Removing the adaptive parameters shown from the gain-scheduled, magnitude-saturation-accommodating, Lyapunov-stability-based (GMS-LS) adaptive controller make it more similar to the MH-96 controller. Neither stage 1 nor stage 2 have the same stability guarantees as the GMS-LS adaptive controller. In stage 2, the controller no longer feeds back α and β measurements from the spherical flow-direction sensor. When the number of adaptive parameters is reduced to three, the same number as the MH-96 controller, the GMS-LS adaptive controller maintains stability in the presence of an 80% unmodeled actuator perturbation.

controller that explicitly accommodates and compensates for these effects would be the controller of choice. As performance limits of flight control expand, the complexities of the underlying model must also increase, necessitating corresponding advances in Lyapunov-stability-based controller designs. Adaptive controllers that accommodate hysteresis such as those in [31] might be needed in such a case. Nonlinear and difficult-to-model aerodynamic effects such as those due to unsteady flow at the shear layer, vortex shedding, hypersonic shock, or turbulence might require neural network-based adaptive control, which attempts to learn the nature of these unknowns [32]–[34]. Additional uncertain effects due to rate saturation, abrupt pilot inputs, and other unmeasurable mechanisms are yet to be explored and are currently active topics of research. It is possible that the methods outlined in [31]–[35] are able to mitigate more known and unknown unknowns. However, all of these approaches are distinct from the MH-96 in that the latter was based on an extrapolation of linear design principles and not grounded in nonlinear stability theory.

The MH-96 adaptive flight control system is an elegant design that accomplished its goal of enforcing performance across all flight conditions. Furthermore, the MH-96 showed that a satisfactory adaptive control system could be designed without having accurate a priori information about the aircraft aerodynamics, and, consequently, aircraft configuration changes could be easily accounted for [40]. However, the MH-96 lacked an analytically based proof of stability, which was highlighted by the fatal crash in 1967. After four decades, the theoretical ground work for applying adaptive control has now made it possible to design adaptive controllers that offer high performance as well as stability guarantees in the presence of uncertainties.

AUTHOR INFORMATION

Zachary T. Dydek (zac@mit.edu) is a Ph.D. candidate in the Department of Mechanical Engineering, MIT, Cambridge, Massachusetts. He received the B.S. in mechanical engineering with a minor in control and dynamical systems from the California Institute of Technology in 2005. His research interests include adaptive control with applications to manned and unmanned aerial vehicles. He received the National Defense Science and Engineering Graduate Fellowship from the Department of Defense in 2006. He is an associate member of Sigma Xi. He can be contacted at MIT, Department of Mechanical Engineering, 77 Massachusetts Ave., Building 3-441, Cambridge, MA 02139 USA.

Anuradha M. Annaswamy received the Ph.D. in electrical engineering from Yale University in 1985. She has been a member of the faculty at Yale, Boston University, and MIT, where she is the director of the Active-Adaptive Control Laboratory and a senior research scientist in the Department of Mechanical Engineering. Her research interests pertain to adaptive control, neural networks, active control of noise in thermofluid systems, active flow control, active emission control, and applications of adaptive control to autonomous vehicles in the air and undersea, as well as automotive systems. She has authored numerous journal and conference papers and coauthored a graduate textbook on adaptive control. She has received several awards including the Alfred Hay Medal from the Indian Institute of Science in 1977, the Stennard Fellowship from Yale University in 1980, the IBM postdoctoral fellowship in 1985, the George Axelby Outstanding Paper award from IEEE Control Systems Society in 1988, and the Presidential Young Investigator award from the National Science Foundation in 1991. She is a Fellow of the IEEE and a member of AIAA.

Eugene Lavretsky is a senior technical fellow of the Boeing Company. He received the M.S. with honors in applied mathematics from the Saratov State University, Russia, in 1983 and the Ph.D. in mathematics from Claremont Graduate University, California, in 2000. He is an associate fellow of AIAA and a Senior Member of IEEE. His research interests include nonlinear dynamics, adaptive control, artificial neural networks, parameter identification, and aircraft flight control.

REFERENCES

[1] D. R. Jenkins. (2000, June). Hypersonics Before the Shuttle: A Concise History of the X-15 Research Airplane (Monographs in Aerospace History: Number 18). NASA, Special Publication SP-2000-4518 [Online]. Available: ntrs.nasa.gov

[2] K. S. Narendra and A. M. Annaswamy, *Stable Adaptive Systems*. Englewood Cliffs, NJ: Prentice-Hall, 1989.

[3] P. A. Ioannou and J. Sun, *Robust Adaptive Control*. Upper Saddle River, NJ: Prentice-Hall, 1996.

[4] H. K. Khalil and J. W. Grizzle, *Nonlinear Systems*. Upper Saddle River, NJ: Prentice-Hall, 1996.

[5] S. P. Karason and A. M. Annaswamy, "Adaptive control in the presence of input constraints," *IEEE Trans. Automat. Contr.*, vol. 39, no. 11, pp. 2325–2330, Nov. 1994.

[6] Z. T. Dydek, H. Jain, J. Jang, A. M. Annaswamy, and E. Lavretsky, "Theoretically verifiable stability margins for an adaptive controller," in *Proc. AIAA Conf. Guidance, Navigation, and Control*, Keystone, CO, Aug. 2006, AIAA-2006-6416.

[7] J. Jang, A. M. Annaswamy, and E. Lavretsky, "Towards verifiable adaptive flight control in the presence of actuator anomalies," in *Proc. Conf. Decision and Control*, San Diego, CA, Dec. 2006, pp. 3300–3305.

[8] B. S. Kim and A. J. Calise, "Nonlinear flight control using neural networks," *J. Guid., Control, Dyn.*, vol. 20, no. 1, pp. 26–33, 1997.

[9] A. J. Calise and R. T. Rysdyk, "Nonlinear adaptive flight control using neural networks," *IEEE Control Syst. Mag.*, vol. 18, no. 6, pp. 14–25, 1998.

[10] J. Boskovic and R. Mehra, "Multiple-model adaptive flight control scheme for accommodation of actuator failures," *J. Guid., Control, Dyn.*, vol. 25, no. 4, pp. 712–724, 2002.

[11] J. Boskovic, L. Chen, and R. Mehra, "Adaptive control design for non-affine models arising in flight control," *J. Guid., Control, Dyn.*, vol. 27, no. 2, pp. 209–217, 2004.

[12] M. Pachter, P. Chandler, and M. Mears, "Reconfigurable tracking control with saturation," *J. Guid., Control, Dyn.*, vol. 18, no. 5, pp. 1016–1022, 1995.

[13] G. Tao, *Adaptive Control Design and Analysis*. New York: Wiley-IEEE Press, 2003.

[14] M. Krstic, P. Kokotovic, and I. Kanellakopoulos, *Nonlinear and Adaptive Control Design*. New York: Wiley, 1995.

[15] R. Isermann, D. Matko, and K. Lachmann, *Adaptive Control Systems*. Upper Saddle River, NJ: Prentice-Hall, 1992.

[16] P. A. Ioannou and K. Tsakalis, "A robust direct adaptive controller," *IEEE Trans. Automat. Contr.*, vol. 31, no. 11, pp. 1033–1043, Nov. 1986.

[17] S. Sastry and M. Bodson, *Adaptive Control: Stability, Convergence, and Robustness*. Englewood Cliffs, NJ: Prentice-Hall, 1989.

[18] J. J. E. Slotine and J. A. Coetsee, "Adaptive sliding controller synthesis for nonlinear systems," *Int. J. Control*, vol. 43, no. 6, pp. 1631–1651, 1986.

[19] B. Egardt and D. Whitacre, *Stability of Adaptive Controllers*. Secaucus, NJ: Springer-Verlag, 1979.

[20] A. Morse, "Global stability of parameter-adaptive control systems," *IEEE Trans. Automat. Contr.*, vol. 25, no. 3, pp. 433–439, 1980.

[21] B. Anderson, T. Brinsmead, F. De Bruyne, J. Hespanha, D. Liberzon, and A. Morse, "Multiple model adaptive control. Part 1: Finite controller coverings," *Int. J. Robust Nonlinear Control*, vol. 10, no. 11–12, pp. 909–929, 2000.

[22] G. C. Goodwin and K. S. Sin, *Adaptive Filtering Prediction and Control*. Englewood Cliffs, NJ: Prentice-Hall, 1984.

[23] I. D. Landau, R. Lozano, and M. M'Saad, *Adaptive Control*. London: Springer, 1998.

[24] G. Feng and R. Lozano, *Adaptive Control Systems*. Oxford, U.K.: Newnes, 1999.

[25] K. J. Åström and B. Wittenmark, *Adaptive Control*. Reading, MA: Addison-Wesley, 1995.

[26] E. Lavretsky and N. Hovakimyan, "Stable adaptation in the presence of actuator constraints with flight control applications," *J. Guid., Control, Dyn.*, vol. 30, no. 2, p. 337, 2007.

[27] M. Sharma, E. Lavretsky, and K. A. Wise, "Application and flight testing of an adaptive autopilot on precision guided munitions," in *Proc. AIAA Guidance Navigation and Control Conf.*, Keystone, CO, Aug. 2006, AIAA-2006-6568, pp. 3416–3421.

[28] K. P. Groves, D. O. Sigthorsson, A. Serraniz, S. Yurkovich, M. A. Bolender, and D. B. Doman, "Reference command tracking for a linearized model of an air-breathing hypersonic vehicle," in *Proc. AIAA Guidance, Navigation, and Control Conf.*, Aug. 2005, AIAA-2005-6144.

[29] T. Gibson, L. G. Crespo, and A. M. Annaswamy, "Adaptive control of hypersonic vehicles in the presence of modeling uncertainties (I)," in *Proc. American Control Conf.*, St. Louis, MO, June 2009, pp. 3178–3183.

[30] J. Jang, A. M. Annaswamy, and E. Lavretsky, "Adaptive control of time-varying systems with gain-scheduling," in *Proc. American Control Conf.*, Seattle, WA, June 2008, pp. 3416–3421.

[31] G. Tao and P. V. Kokotovic, "Adaptive control of plants with unknown hystereses," *IEEE Trans. Automat. Contr.*, vol. 40, no. 2, pp. 200–212, Feb. 1995.

[32] R. T. Anderson, G. Chowdhary, and E. N. Johnson, "Comparison of RBF and SHL neural network based adaptive control," *J. Intell. Robot. Syst.*, vol. 54, no. 1–3, pp. 183–199, Mar. 2009.

[33] N. Nguyen, K. Krishnakumar, J. Kaneshige, and P. Nespeca, "Flight dynamics and hybrid adaptive control of damaged aircraft," *J. Guid., Control, Dyn.*, vol. 31, no. 6, pp. 1837–1838, Nov.–Dec. 2008.

[34] Y. Shin, A. J. Calise, and M. D. Johnson, "Adaptive control of advanced fighter aircraft in nonlinear flight regimes," *J. Guid., Control, Dyn.*, vol. 31, no. 5, pp. 1464–1477, Sept.-Oct. 2008.

[35] S. Ferrari and R. F. Stengel, "Online adaptive critic flight control," *J. Guid., Control, Dyn.*, vol. 27, pp. 777–786, 2004.

[36] W. H. Dana. (1993). The X-15 lessons learned. NASA Dryden Res. Facility, Tech. Rep. AIAA-93-0309 [Online]. Available: ntrs.nasa.gov

[37] J. Brinker and K. Wise, "Flight testing of reconfigurable control law on the X-36 tailless aircraft," *J. Guid., Control, Dyn.*, vol. 24, no. 5, pp. 903–909, 2001.

[38] D. Ward, J. Monaco, and M. Bodson, "Development and flight testing of a parameter identification algorithm for reconfigurable control," *J. Guid., Control, Dyn.*, vol. 21, no. 6, pp. 948–956, 1998.

[39] D. R. Jenkins, *X-15: Extending the Frontiers of Flight*. Washington, DC: NASA, 2007.

[40] Staff of the Flight Research Center. (1971, Mar.). Experience with the X-15 adaptive flight control system. NASA, Flight Res. Center, Edwards, CA, Tech. Note D-6208 [Online]. Available: ntrs.nasa.gov

[41] L. W. Taylor, Jr. and E. J. Adkins. (1964, Apr.). Adaptive flight control systems—pro and con. NASA, Flight Res. Center, Edwards, CA, Tech. Memo. X-56008 [Online]. Available: ntrs.nasa.gov

[42] K. J. Åström, "Adaptive control around 1960," in *Proc. Conf. Decision and Control*, New Orleans, LA, Dec. 1995, pp. 2784–2789.

[43] B. Boskovich and R. Kaufmann, "Evolution of the Honeywell first-generation adaptive autopilot and its applications to F-94, F-101, X-15, and X-20 vehicles," *J. Aircraft*, vol. 3, no. 4, pp. 296–304, 1966.

[44] M. O. Thompson and J. R. Welsh, "Flight test experience with adaptive control systems," in *Proc. Advanced Control System Concepts, AGARD*, Jan. 1970, pp. 141–147.

[45] L. W. Taylor, Jr. and G. B. Merrick. (1962, Mar.). X-15 airplane stability augmentation system. NASA, Flight Res. Center, Edwards, CA, Tech. Note D-1157 [Online]. Available: ntrs.nasa.gov

[46] E. C. Holleman. (1966, Feb.). Control experiences of the X-15 pertinent to lifting entry. NASA, Flight Res. Center, Edwards, CA, Tech. Note D-3262 [Online]. Available: ntrs.nasa.gov

[47] B. L. Stevens and F. L. Lewis, *Aircraft Control and Simulation*. New York: Wiley, 1992.

[48] R. C. Nelson, *Flight Stability and Automatic Control*. New York: McGraw-Hill, 1989.

[49] R. B. Yancey, H. A. Rediess, and G. H. Robinson. (1962, Jan.). Aerodynamic-derivative characteristics of the X-15 research airplane as determined from flight tests for Mach numbers from 0.6 to 3.4. NASA, Flight Res. Center, Edwards, CA, Tech. Note D-1060 [Online]. Available: dtrs.dfrc.nasa.gov

[50] R. B. Yancey. (1964, Nov.). Flight measurements of stability and control derivatives of the X-15 research airplane to a Mach number of 6.02 and an angle of attack of 25°. NASA, Flight Res. Center, Edwards, CA, Tech. Note D-2532 [Online]. Available: ntrs.nasa.gov

[51] H. J. Walker and C. H. Wolowicz. (1962, Mar.). Stability and control derivative characteristics of the X-15 airplane. NASA, Flight Res. Center, Edwards, CA, Tech. Memo. X-714 [Online]. Available: ntrs.nasa.gov

[52] E. J. Saltzman and D. J. Garringer. (1966, Mar.). Summary of full-scale lift and drag characteristics of the X-15 airplane. NASA, Flight Res. Center, Edwards, CA, Tech. Note D-3343 [Online]. Available: ntrs.nasa.gov

[53] H. J. Walker and C. H. Wolowicz. (1960, Aug.). Theoretical stability derivatives for the X-15 research airplane at supersonic and hypersonic speeds including a comparison with wind tunnel results. NASA, Flight Res. Center, Edwards, CA, Tech. Memo. X-287 [Online]. Available: ntrs.nasa.gov

[54] C. R. Jarvis and E. J. Adkins. (1964, Apr.). Operational experience with the X-15 reaction controls. NASA, Flight Res. Center, Edwards, CA, Tech. Memo. X-56002 [Online]. Available: ntrs.nasa.gov

[55] C. R. Jarvis and W. P. Lock. (1965, June). Operational experience with the X-15 reaction control and reaction augmentation systems. NASA, Flight Res. Center, Edwards, CA, Tech. Note D-2864 [Online]. Available: ntrs.nasa.gov

[56] M. A. Bolender and D. B. Doman, "A non-linear model for the longitudinal dynamics of a hypersonic air-breathing vehicle," in *Proc. AIAA Guidance, Navigation, and Control Conf.*, Aug. 2005, AIAA-2005-6255.

[57] Staff of the Flight Research Center. (1965, Oct.). Progress of the X-15 research airplane program. NASA, Flight Res. Center, Edwards, CA, Special Publication SP-90 [Online]. p. 74. Available: ntrs.nasa.gov

[58] J. G. Ziegler and N. B. Nichols, "Optimum settings for automatic controllers," *ASME Trans.*, vol. 65, pp. 433–444, 1942.

[59] L. W. Taylor, Jr. (1961, Nov.). Analysis of a pilot-airplane lateral instability experienced with the X-15 airplane. NASA, Flight Res. Center, Edwards, CA, Tech. Note D-1059 [Online]. Available: ntrs.nasa.gov

[60] R. A. Hess, "Feedback control models," in *Handbook of Human Factors*, G. Salvendy, Ed. New York: Wiley, 1987, pp. 1212–1242.

[61] R. A. Hess, "A model-based theory for analyzing human control behavior," in *Advances in Man-Machine Systems Research*, vol. 2, W. B. Rouse, Ed. London, England: JAI Press, 1985, pp. 129–176.